

Pixelated Phase-Mask Dynamic Interferometer

James Millerd, Neal Brock, John Hayes, Michael North-Morris, Matt Novak and James Wyant

4D Technology Corporation, 3280 E. Hemisphere Loop, Suite 146, Tucson, AZ 85706
(520) 294-5600, (520) 294-5601 fax, james.millerd@4dtechnology.com

We demonstrate a new type of spatial phase-shifting, dynamic interferometer that can acquire phase-shifted interferograms in a single camera frame. The interferometer is constructed with a pixelated phase-mask aligned to a detector array. The phase-mask encodes a high-frequency spatial interference pattern on two collinear and orthogonally polarized reference and test beams. The phase-difference between the two beams can be calculated using conventional N-bucket algorithms or by spatial convolution. The wide spectral response of the mask and true common-path design permits operation with a wide variety of interferometer front ends, and with virtually any light source including white-light.

Introduction

Phase-stepping interferometry is an established method for measuring a variety of physical parameters ranging from the surface figure of mirrors to the displacement of solid objects.¹ Phase-shift interferometers typically have an element in the path of the reference wavefront that introduces three or more known phase steps or shifts. By detecting the intensity pattern with a detector at each of the phase shifts, the phase distribution of the object wavefront can be quantitatively calculated independent of any attenuation in either of the reference or object wavefronts. Both continuous phase gradients and discontinuous phase gradients (speckle waves) can be measured using this technique.

Phase shifting of a light beam can either be accomplished by sequentially introducing a phase step (temporal phase shifting) or by splitting the beam into parallel channels for simultaneous phase steps (spatial phase shifting). Spatial phase shifting achieves data acquisition in a time several orders of magnitude less than temporal phase shifting, thus offering significant immunity to vibration.

Several methods of spatial phase shifting have been developed over the years. Smythe and Moore¹ described a spatial phase-shifting method where conventional beam splitters and polarization optics are used to produce three or four phase-shifted images onto as many cameras for simultaneous detection. Koliopoulos² also described a system using multiple cameras to detect multiple interferograms. While functional, these methods require relatively complex optical and electronic arrangements and have had only limited commercial success.

Several authors describe methods that employ diffractive elements to simultaneously image three or more interferograms onto a single sensor.^{3,4,5,6} These methods are considerably more compact and less expensive than multi-camera arrangements; however, they operate only over a limited wavelength range due to dispersion and chromatic distortion inherent in their design. Thus, they are not capable of working with white light or short coherence-length source interferometers.

Spatial phase shifting has also been accomplished using a tilted reference wave to induce a spatial carrier frequency to the pattern.^{7,8} The spatial carrier method inherently requires a path-length difference of at least many hundreds of waves between the test and reference wavefronts, thereby precluding the use of white light. In addition, interferometers employing this arrangement must utilize high precision optics to avoid introducing aberrations between the two non-common path beams.

In this paper we describe an optical system that obtains spatial phase-shifted interferograms on a single detector array but overcomes many of the limitations of previous techniques. The method has the following advantages:

- 1) A true common path arrangement permits the use of broadband or white light and minimizes aberrations,
- 2) Extremely compact design,
- 3) Achromatic over a very wide range,
- 4) Fixed spatial interference pattern results in fast processing.

Phase Sensor Configuration

The heart of the system lies in a pixelated phase-mask where each pixel has a unique phase-shift. By arranging the phase-steps in a repeating pattern, fabrication of the mask and processing of the data can be simplified. A small number of discrete steps can be arranged into a “unit cell” which is then repeated contiguously over the entire array. The unit cell can be thought of as a super-pixel; the phase across the unit cell is assumed to change very little. By providing at least three discrete phase-shifts in a unit cell, sufficient interferograms are produced to characterize a sample surface using conventional interferometric algorithms. Figure 1 illustrates a unit cell comprised of four discrete phase steps. Other combinations are possible; however, four phase steps provide optimal sampling. The example shows the phase-steps are in quadrature. For best resolution, a one-to-one correspondence is preferably used between the phase-mask and the detector pixels.

The overall system concept is shown in Figure 1. and consists of a polarization interferometer that generates a reference wavefront R and a test wavefront T having orthogonal polarization states (which can be linear as well as circular) with respect to each other; a pixelated phase-mask that introduces an effective phase-delay between the reference and test wavefronts at each pixel and subsequently interferes the transmitted light; and a detector array that converts the optical intensity sensed at each pixel to an electrical charge. The pixelated phase-mask and the detector array may be located in substantially the same image plane, or positioned in conjugate image planes.

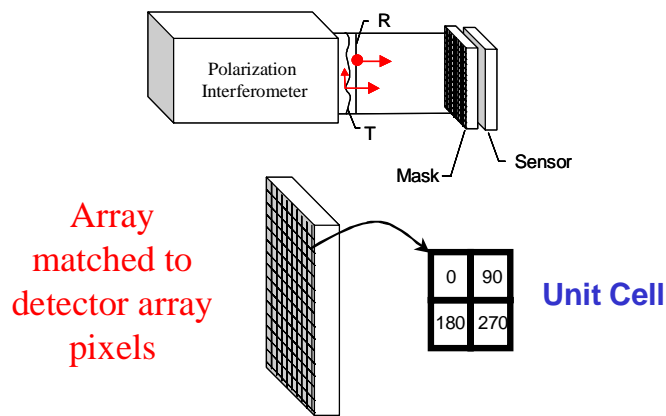


Figure 1. Basic concept for the pixelated phase-mask dynamic interferometer.

In principle, a phase-mask shown in Figure 1 could be constructed using an etched birefringent plate, however, such a device is difficult to manufacture accurately. An alternative approach is to use an array of micropolarizers. Kothiyal and Delisle⁹ showed that the intensity of two beams having orthogonal circular polarization (i.e., right-hand circular and left-hand circular) that are interfered by a polarizer is given by

$$I(x, y) = \frac{1}{2} \left(I_r + I_s + 2\sqrt{I_r I_s} \cos(\Delta\phi(x, y) + 2\alpha_p) \right) \quad (1.)$$

where α_p is the angle of the polarizer with respect to the x, y plane. The basic principle is illustrated in Figure 2. From this relation it can be seen that a polarizer oriented at zero degrees causes interference between the in-phase (i.e., 0°) components of the incident reference and test wavefronts R and T. A polarizer oriented at 45 degrees interferes the in-phase quadrature (i.e., 90°) component between the incident reference and test wavefronts R and T. A polarizer oriented at 90 degrees interferes the out-of-phase (i.e., 180°) component between the incident reference and object wavefronts R and T. Finally, a polarizer oriented at 135 degrees interferes the out-of-phase quadrature (i.e., 270°) component between the incident reference and test wavefronts R and T.

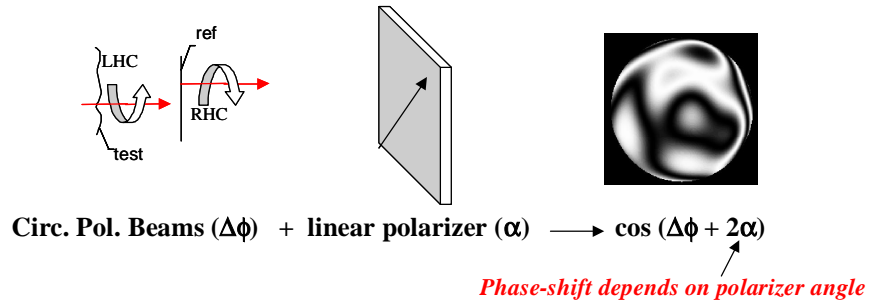


Figure 2. Basic principal of pixelated phase-shift inteferometer.

The basic principle can be extended to an array format so that each pixel has a unique phase-shift transfer function. Some possible methods to construct the pixelated phase-mask are shown in Figure 3. Nordin et al.¹⁰ describe the use of micropolarizer arrays made from fine conducting wire arrays for imaging polarimetry in the near infrared spectrum. Recently, the use of wire grid arrays has also been demonstrated in the visible region of the spectrum.¹¹ The planar nature of the conducting strip structure permits using it as a polarizer over an extremely wide incident angle, including zero degrees, and over a broad range of wavelengths, provided the period remains much less than the wavelength. Other investigators also describe the use of patterned multi-level organic thin films for imaging polarimetry in the visible spectral range.¹²

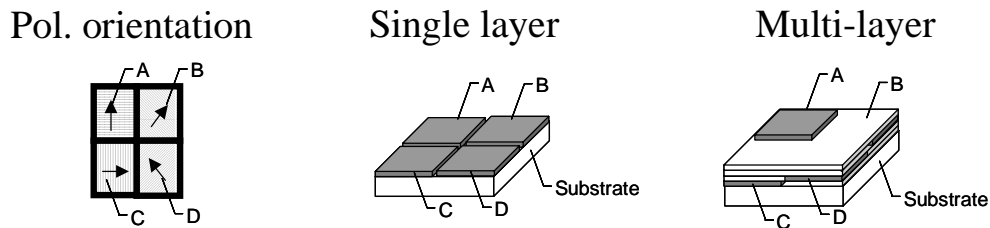


Figure 3. Unit cell orientation and construction of polarizer elements.

For circular polarized input light, the micropolarizer array can be used directly. For linear polarized input light, which is more typical of polarization interferometers, a quarter-wave retarder plate can be used in combination with the micropolarizer array as shown in Figure 4. For convenience, the quarter-wave retarder may be adjoined to the oriented polarizer array to form the pixelated phasemask; however, the two elements do not need to be in contact and could be separated by a substantial distance or separated by other imaging optics.

Helen et al.¹³ demonstrated that by combining conventional half-wave and quarter-wave plates in series an effective quarter-wave plate may be constructed that works over a broad wavelength range. Thus, the quarter-wave retarder may be constructed by abutting several conventional half-wave and quarter-wave retardation plates in combination. This permits operation over a broad range of wavelengths or with a single broadband source.

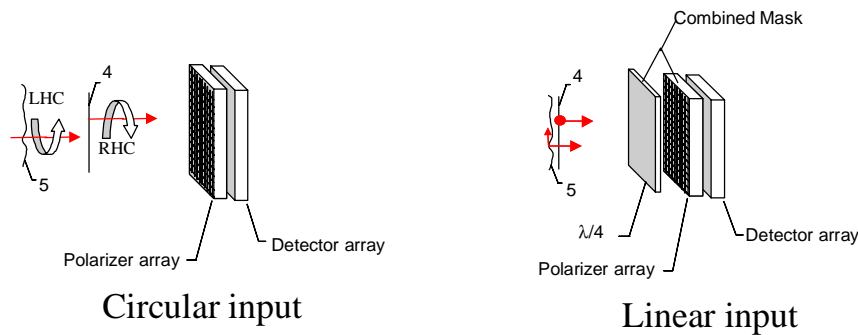


Figure 4. Two phasemask arrangements for circular and linear input polarizations.

Data Processing

The effective phase-shift of each pixel of the polarization phase-mask can have any spatial distribution; however, it is highly desirable to have a regularly repeating pattern. A preferred embodiment for the polarization phase-mask is based on an arrangement wherein neighboring pixels are in quadrature or out-of-phase with respect to each other; that is, there is a ninety-degree or one hundred eighty degree relative phase shift between neighboring pixels.

Figure 3 illustrates one possible way of arranging the polarization phase-mask and detector pixels and for processing the measured data. A preferred orientation for arranging the pixel masks when using a CCD sensor is to alternate the out-of-phase signals along columns. For example, channels 0 and 180 can be arranged in an alternating pattern along one column, as shown in Figure 1. Likewise 90 and 270 can be arranged along adjacent columns. At short exposures, CCDs are prone to large smear signals, an additive or offset error proportional to the total fluence integrated along the column. By arranging the pixel masks such that out-of-phase pixels are lined up in a column, the smear signal is constant regardless of input phase, this minimizing the phase-dependent error due to sensor smear. The capital letters in Figure 3, A, B, C and D, represent different transfer functions as a result of the filtering from the pixelated phase-mask. The signal measured at each sensor pixel is given by its transfer function, the phase-difference between the reference and test beams, and the amplitude of each beam. For example, one possible configuration is,

$$A(x, y) = \frac{1}{2} \left(I_r + I_s + 2\sqrt{I_r I_s} \cos(\Delta\phi(x, y)) \right) \quad (2.a)$$

$$B(x, y) = \frac{1}{2} \left(I_r + I_s + 2\sqrt{I_r I_s} \cos\left(\Delta\phi(x, y) + \frac{\pi}{2}\right) \right) \quad (2.b)$$

$$C(x, y) = \frac{1}{2} \left(I_r + I_s + 2\sqrt{I_r I_s} \cos(\Delta\phi(x, y) + \pi) \right) \quad (2.c)$$

$$D(x, y) = \frac{1}{2} \left(I_r + I_s + 2\sqrt{I_r I_s} \cos\left(\Delta\phi(x, y) + \frac{3\pi}{2}\right) \right) \quad (2.d)$$

wherein $I_r(x,y)$ and $I_s(x,y)$ are the intensities of the reference and test wavefronts R and T at each x, y coordinate in the image, respectively, and $\Delta\phi(x,y)$ is the optical path difference between the reference and test wavefronts.

Multiple interferograms can thus be synthesized by combining pixels with like transfer functions. To generate a continuous fringe map that opticians are accustomed to viewing for alignment, pixels with transfer functions can be combined into a single image or interferogram. For example all the pixels with transfer function A can be combined into a single image. The resulting interferogram can be displayed on a screen in real-time. The B, C, and D pixels can be similarly combined to produce corresponding interferograms. The resulting interferograms have a total number of pixels equal to $(n \times m)/N$, where n and m are the numbers of pixels in the detector array in the x and y directions, respectively, and N is the number of different discrete phase-shift elements in the pixelated phase mask. In the above examples N is equal to four. The resulting four interferograms can be processed by a variety of algorithms that are well-known in the art for calculating phase difference and modulation index.¹⁴ For example, a possible implementation for measuring phase difference is a simple four-bucket algorithm, e.g.,

$$\phi(x, y) = ATAN\left(\frac{(C(x, y) - A(x, y))}{(D(x, y) - B(x, y))}\right) \quad (3.)$$

where the values A, B, C, and D are taken from adjacent neighboring pixels. Similarly, a modulation index map can be generated (similar to the phase-difference map) using the formula

$$\gamma(x, y) = \frac{2\sqrt{(A(x, y) - C(x, y))^2 + (D(x, y) - B(x, y))^2}}{D(x, y) + B(x, y) + A(x, y) + C(x, y)} \quad (4.)$$

An alternative method for calculating the phase difference at each spatial coordinate is to combine the measured signals of neighboring pixels in a fashion similar to a windowed convolution algorithm. This method provides an output phase-difference map having a total number of pixels equal to $(n-W)$ times $(m-V)$, where W and V are the sizes of the correlation window in the x and y directions, respectively. Thus, the resolution of the phasemap is close to the original array size, although the spatial frequency content has been somewhat filtered by the convolution process.

A comparison of the two approaches was done by numerical analysis. Figure 5 shows the residual phase-dependent error for the case of the simple 4 bucket approach (i.e. parsed into 4 interferograms and calculated with Eqn. 3) and the 3x3 convolution approach. A four fold reduction in phase error can be seen, even for the case of high local phase slope (10 pixels per fringe). Thus, the convolution approach provides a higher data array size and lower phase-dependent error. The cost of the convolution approach is processing time, however, we can achieve processing times of several frames per second for a data array of 1 million pixels, using a 2GHz Pentium computer.

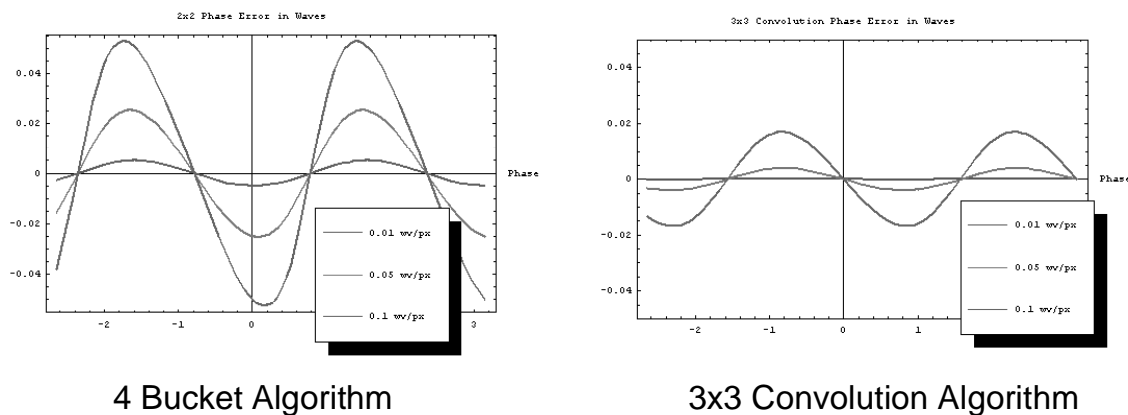


Figure 5. Comparison of a simple 4 bucket (parsed) algorithm to a windowed 3 x 3 convolution. The 3x3 convolution method has 4 times lower phase-dependent error and results in four times larger data array, at the expense of computation time.

Interferometer Configurations

The pixelated phase-mask can be configured to measure various parameters. As shown below, the pixelated phasemask may be configured to measure optical phase-difference between a reference and a test wavefront in real time; to perform profilometry of an object (that is, to measure the absolute three-dimensional profile of a solid object) with a dynamic range of sub-angstrom to centimeters; to measure the displacement (e.g., thermal strain or vibration) of an object; to measure the wavefront quality of light sources, such as in optical data-storage pickup/transmit assemblies; and to measure flow parameters in a multiphase environment. Examples of such flow parameters include the concentration of selected gaseous species, temperature distributions, particle and droplet size distributions, density, and so on.

One type of measurement system is illustrated in Figure 6, wherein the pixelated phase-mask is used in conjunction with a Twyman-Green interferometer. A linearly polarized beam from a light source is combined with a half-wave plate to produce a linearly polarized beam of desired polarization angle directed to a polarizing beam splitter, which in turn generates a reference beam directed toward a reference surface and a test beam directed toward a test surface that are linearly polarized along orthogonal axes. Quarter-wave plates are used to rotate the test and reference beams after reflection while retaining their mutually orthogonal linear polarization states, so that they may be transmitted through and reflected from the beam splitter, respectively, toward the relay optics. A coupling lens is used in combination with the test surface to return a substantially collimated test beam.

The imaging system is comprised of an input lens, an aperture, and an exit lens to relay the reference wavefront and the test wavefront onto the pixelated phase-mask and the detector array. The focal length of the lenses and the spacing between lenses are adjusted properly to form an image of the input pupil plane at the location of the pixelated phase-mask. The aperture is preferably selected so that the diffraction-limited spot size at the pixelated phase-mask is approximately 2 effective pixels in diameter in order to avoid aliasing of the interference pattern spatial frequency. This selection of the aperture ensures that spatial frequencies higher than the pixel spacing are not present in the final interference pattern.

An alternative arrangement (not shown), is to position the pixelated phase-mask at the input pupil plane and relay optics are used to re-image the light transmitted through the pixelated phase-mask onto the detector array. One advantage of this arrangement is the ability to scale the “effective pixel size” of the detector array as desired relative to the pixelated phase-mask by introducing magnification in the relay optics. Thus, the physical pitch (pixel spacing) of the pixelated phase-mask and the detector array do not need to be equal. In addition, the pixelated phase-mask and the detector array can be located in conjugate image planes to within an arbitrarily high degree.

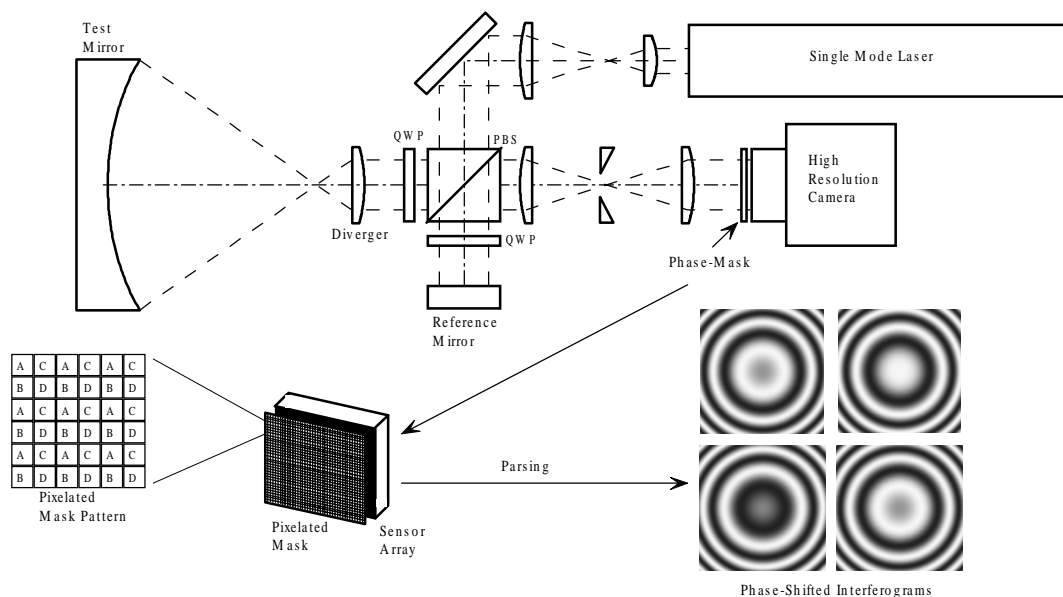


Figure 6. Twyman-Green configuration for pixelated interferometer.

Figure 7 illustrates a measurement system configured to function as a wavefront sensor. Wavefront sensors are used to measure, for example, pressure, temperature, or density gradients in transparent solids, liquids, and gases, as well as the quality of optical beams emitted from lasers. The configuration is based on the use of a polarizing point-diffraction plate (PDP).¹⁵ The input light L is received for testing through an entrance pupil and a sample wavefront S is produced by an objective lens (which may consist of multiple elements) by focusing the light L onto a polarizing point diffraction plate. The light L may be narrow or broadband. The PDP is typically positioned perpendicular to the direction of light propagation and is used to produce two mutually orthogonal, polarized output wavefronts that propagate along a common path. The first wavefront T (the test wavefront) is a copy of the sample wavefront S . The second wavefront R is a spherical beam used as a reference wavefront because of its orthogonal polarization with respect to the test wavefront. A mechanism may be coupled to the PDP to enable its rotation about the optical axis and, if the input polarization is linear, change the power ratio of the reference and test beams. A lens system collimates both the test and reference wavefronts T, R and delivers them to the pixelated phase-mask for processing and analysis.

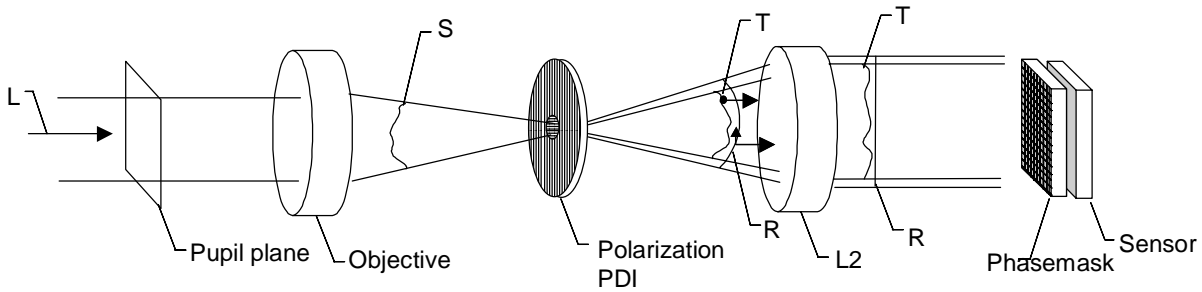


Figure 7. Pixelated phasemask used in combination with a polarization point diffraction element to produce a compact wavefront sensor.

Figure 8 illustrates another interferometer configured to function as a strain sensor. Strain sensors are useful in measuring, for example, small deformations of an object due to acoustical, mechanical or thermal stress. The illumination unit and a corresponding expansion lens are adapted so that they may be positioned at an arbitrary angle γ relative to the test object and adjust the illumination to fill the area of interest. Imaging lens is used to collect light scattered from the test object and produce an image at the polarization phase-mask and detector array. An aperture is used to control the speckle size at the image. The reference beam R is generated using a beam splitter and combined with the test beam T at polarizing beamsplitter. The strain sensor is primarily sensitive to motion or deformation of the test object along the bisector of the angle γ . Thus, if γ is selected to be nearly equal to zero, the sensor is primarily sensitive to motion out of the plane of the sample object (i.e., along z).

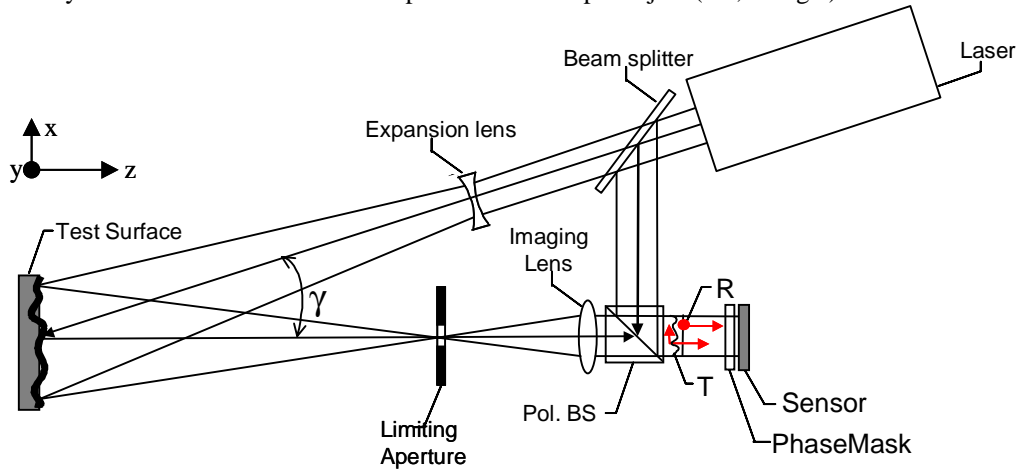


Figure 8. Optical layout for measuring surface strain.

For comparing two states of the system, such necessary for the strain measurement or to subtract background phase noise from the system, the phase difference mode can be used. Phase may be calculated according to the well known relation:

$$\Delta\Phi(x,y) = \tan^{-1}[X(x,y) \div Y(x,y)], \quad (5.)$$

where:

$$X(x,y) = [D_0(x,y) - B_0(x,y)] * [A_1(x,y) - C_1(x,y)] - [D_1(x,y) - B_1(x,y)] * [A_0(x,y) - C_0(x,y)],$$

$$Y(x,y) = [A_0(x,y) - C_0(x,y)] * [A_1(x,y) - C_1(x,y)] + [D_0(x,y) - B_0(x,y)] * [D_1(x,y) - B_1(x,y)],$$

A_0, B_0, C_0, D_0 are the baseline images captured, and

A_1, B_1, C_1, D_1 are the images captured for comparison.

The three dimensional shape of an object can be determined by using two-color interferometry. A single set of four phase-shifted interferograms is captured at wavelength λ_0 (A₀-D₀) and a second set of phase-shifted interferograms is captured at wavelength λ_1 (A₁-D₁). The relative distance to the object (or range) is calculated by

$$R(x, y) = \frac{\lambda^2}{4\pi \Delta\lambda} \tan^{-1} \left(\frac{X(x, y)}{Y(x, y)} \right), \quad (6.)$$

where $\Delta\lambda = |\lambda_0 - \lambda_1|$. Noise in the image can be significantly reduced using a weighted spatial average over neighboring pixels. This can be accomplished by:

$$R(x, y) = \frac{\lambda^2}{4\pi \Delta\lambda} \tan^{-1} \left(\frac{\sum_{x, y \in \delta} X(x, y)}{\sum_{x, y \in \delta} Y(x, y)} \right), \quad (7.)$$

where the sums are performed over the range of δ nearest neighbors. Because of the modulo 2π behavior of the arctangent function, the range is wrapped (ambiguous) beyond the so-called synthetic wavelength

$$\lambda_s = \frac{\lambda^2}{\Delta\lambda}. \quad (8.)$$

Therefore, the well known process of spatial phase unwrapping can be used to remove the discontinuous steps and perform quantitative analysis of the images. Alternatively, it is possible to use multiple synthetic wavelengths and incrementally add the range distance.¹⁶ The overall range is then given by:

$$R'(x, y) = \sum_m \frac{R_{\Delta\lambda m}(x, y)}{m}, \quad (9.)$$

where m is the number of wavelength steps used and $R_{\Delta\lambda m}$ is the range measured with a frequency tuning of $\Delta\lambda/m$. Implied in this method is that no single measurement should have a phase value greater than 2π , which can place a restriction on the maximum size of the object that can be measured.

Results

We constructed a pixelated phase-mask sensor using a planar deposition technique. The pixel pitch of the mask and CCD was 9 microns, and was 1000x1000 pixels wide. The pixelated phase-mask was positioned directly in front of a CCD array, aligned and bonded to the carrier package using an ultra-low expansion epoxy.

Figure 9 shows data measured from a pixelated phasemask sensor configured as a Twyman-Green interferometer. Two flat mirrors were used as the reference and test objects, respectively. The angle between the mirrors was adjusted to give several fringes of tilt. The image shows a magnified area of 24 x 17 pixels from the CCD array. The greyscale of the image corresponds to the measured intensity at each pixel. The high contrast between adjacent pixels demonstrates the ability to accomplish discrete spatial phase shifting at the pixel level. Every 4th pixel was combined to generate a continuous fringe map or interferogram. The synthetic fringe map shows excellent contrast across the whole array. We measured good fringe contrast with up to 170 fringes of tilt in each direction before the onset of unwrapping errors.

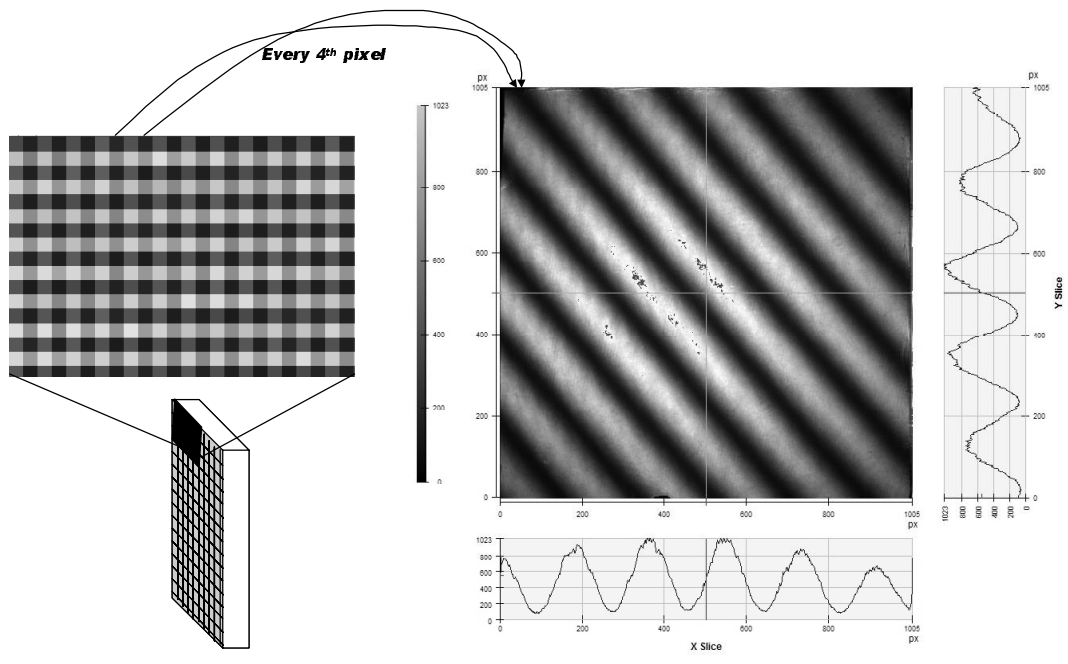


Figure 9. Actual measurements made with the interferometer of Figure 6. Checked pattern is a magnified grayscale image showing 24 x 17 pixels. The Fringe pattern is synthesized by selecting every fourth pixel.

A wrapped fringe map was calculated using the 3x3 convolution approach. The resulting fringe map is shown in Figure 10. The resulting map has 974 x 980 pixels, just under the actual CCD dimensions. The CCD and mask combination was cycled over a wide temperature range and exhibited good thermal stability.

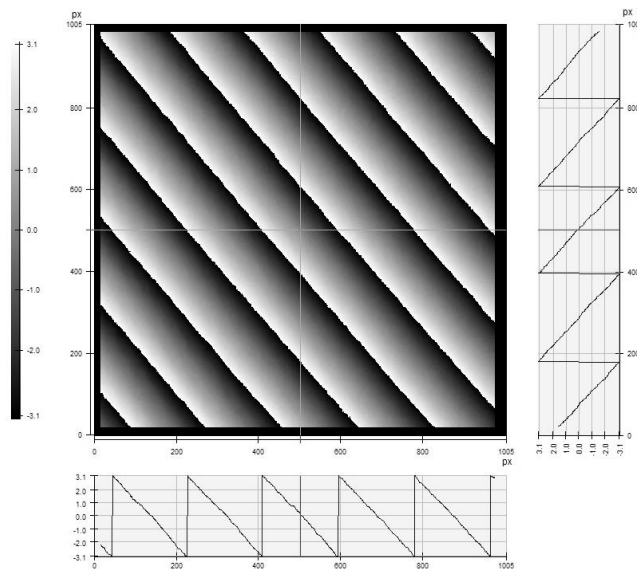


Figure 10. Sawtooth fringe map generated with the pixelated phasemask and the interferometer of Figure 6. Test object was a flat mirror tilted with respect to the reference beam.

We performed a series of measurements to determine the instrument repeatability. 10 measurements were made of the test mirror, each measurement consisting of 16 averages. The results of the study are shown in Table 1. The uncalibrated accuracy, defined as the pixel-wise average of all 160 measurements, was limited mainly to the

polarization beamsplitter. Precision, defined as the average deviation of each measurement subtracted from the calibrated surface on a pixel-by-pixel basis, was below 1 milliwave rms. Repeatability, defined as the standard deviation of the 10 measurements, was below 1/10th milliwave rms.

Uncalibrated Accuracy	0.0039 waves rms
Precision	0.0007 waves rms
Repeatability	0.00008 waves rms

Table 1. Measured performance for the pixelated phasemask interferometer using a flat reference.

To illustrate the use of the pixelated phase-mask sensor for other applications, we replaced the test object with a rough ground finish, aluminum surface from a hard disk drive assembly. We induced changes by tilting the surface and recording interferograms before and after. Figure 11 shows measurement results with 7 fringes of tilt. The results are typical of ESPI measurements made using the carrier fringe technique.¹⁷

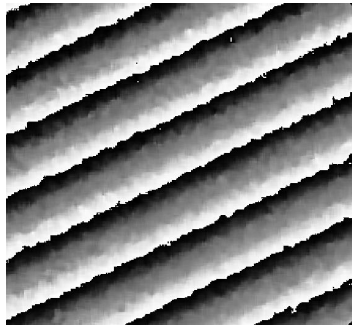


Figure 11. Wrapped fringes measured using the speckle interferometer of Figure 8. The test surface was an aluminum transducer suspension assembly from a hard disk drive that was tilted between measurements.

We also measured a 6 inch diameter mirror that had a 2meter radius of curvature. The mirror and the interferometer were located on separate tables and there was no active vibration isolation. The measurement results are shown in Figure 12. This type of measurement (across two non-isolated tables) is not possible with conventional temporal phase-shifting interferometers.

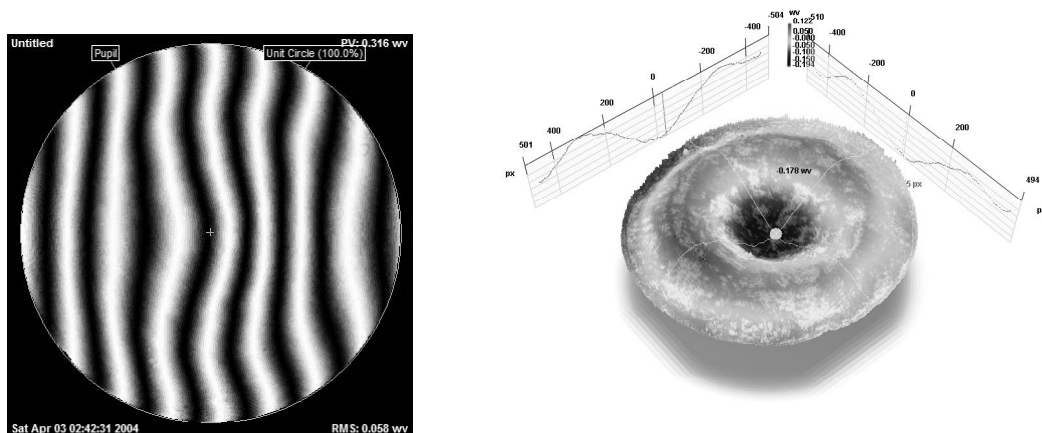


Figure 12. Measurement of a spherical lens with a 2 meter radius of curvature. Mirror and interferometer were located on two separate, non-vibration isolated tables.

Conclusion

We have demonstrated a new type of spatial phase-shift interferometer that uses a pixelated phase-mask to impart a discrete phase-shift on each pixel. The phase-mask is comprised of a micropolarizer array and can work with any type polarization interferometer to measure a variety of physical properties. The unique configuration overcomes many of the limitations of previous single frame, phase-shift interferometer techniques. In particular it has a true common path arrangement, which permits the use of broadband or white light, extremely compact design, and is achromatic over a very wide range. The fixed spatial interference pattern results in fast processing that does not compromise spatial resolution. We demonstrated the pixelated phase-mask in a Twyman-Green type interferometer, showed excellent repeatability and the ability to measure over long paths and diffuse surfaces.

¹ R. Smythe, R. Moore "Instantaneous phase measuring interferometry" *Optical Engr.* Vol. 23, No. 4, p. 361, 1984.

² C. Koliopoulos, "Simultaneous phase shift interferometer," SPIE Vol. 1531, p 119-127 *Advanced Optical Manufacturing and Testing II*, 1991.

³ B. Barrientos et. al., "Transient Deformation Measurement with ESPI Using a Diffractive Optical Element for Spatial Phase-stepping," *Fringe*, p 317-8, Akademie Verlag (1997)

⁴ A. Hettwer, J. Kranz, J. Schwider, "Three channel phase-shifting interferometer using polarization-optics and a diffraction grating," *Optical Engineering*, pp 960, Vol. 39 No. 4, April 2000.

⁵ J. E. Millerd and N. J. Brock, US Patent No. 6,304,330 and 6,522,808 "*Methods and Apparatus for splitting imaging and measuring wavefronts in interferometry*," Oct 16, 2001

⁶ B. B. Garcia, A. J. Moore, C. Perez-Lopez, L. Wang, and T. Tschudi, "Spatial phase-stepped interferometry using a holographic optical element," *Opt. Eng.* 38(12) p2069-2074 1999.

⁷ M. Kuchel, "The new Zeiss interferometer," SPIE Vol. 1332 *Optical Testing and Metrology III: Recent Advances in Industrial Optical Inspection*, p655-663, 1990.

⁸ K. Freischlad, R. Eng, J. Hadaway, "Interferometer for testing in vibration environments" *SPIE Proc.*

⁹ P. Kothiyal and R. Delisle, "Shearing interferometer for phase shifting interferometry with polarization phase shifter," *Applied Optics* Vol. 24, No. 24, pp. 4439-4442, 1985.

¹⁰ Nordin, et. al., "Micropolarizer array for infrared imaging polarimetry," *J. Opt. Soc. Am A*, Vol. 16, No. 5, 1999.

¹¹ See for example, U.S. Patents No. 6,108,131, No. 6,122,103, No. 6,208,463 and No. 6,243,199.

¹² J. Gou et. al., "Fabrication of thin-film micropolarizer arrays for visible imaging polarimetry," *Applied Optics* Vol. 39, No. 10, 2000.

¹³ Helen, et. al., "Achromatic phase-shifting by a rotating polarizer" *Optics Communications* 154, p249-254, 1998

¹⁴ see for example, *Interferogram Analysis for Optical Testing*. Malacara et. al. Marcel Decker, Inc. New York, 1998.

¹⁵ J. Millerd, et. al. "Instantaneous phase-shift point-diffraction interferometer." *SPIE Proc.* Same Volume, paper 5531-31.

¹⁶ J.M. Huntley and H.O. Saldner, "Profilometry using temporal phase unwrapping and a spatial light modulator-based fringe projector," *Opt. Eng.* 36 pp. 610-615 (1997).

¹⁷ J. Burke and H. Helmers, "Spatial versus temporal phase shifting in electronic speckle-pattern interferometry: noise comparison in phase maps," *Appl. Opt.* 39, n 25. p4598-4605, 2000.